Four-body postcollision interaction and two-photon pathways in neon double-core-hole states

Abhishek Verma,[1,2,3] Renaud Guillemin,[1] Ralph Püttner,[4] Iyas Ismail,[1] Dimitris Koulentianos,[5] Gilles Doumy,[5] Tatiana Marchenko,[1] Oksana Travnikova,[1] Dawei Peng,[1,6] Nicolas Velasquez,[1,7] Anthony Ferté,[1,8] Francis Penent,[1] Florian Trinter,[7] Linda Young,[5,9] Stephen H. Southworth,[5] Alberto De Fanis,[6] Thomas Baumann,[6] Simon Dold,[6] Markus Ilchen,[6,8,10] Daniel Rivas,[6] Edwin Kukk,[1,11] Stéphane Carniato,[1] Tommaso Mazza,[6] Michael Meyer,[6] John Bozek,[2,*] and Marc Simon[1,12,†]

[1]*Sorbonne Université, CNRS, UMR 7614, Laboratoire de Chimie Physique-Matière et Rayonnement, F-75005 Paris, France*
[2]*Synchrotron SOLEIL, L'Orme des Merisiers, Saint-Aubin, F-91192 Gif-sur-Yvette, Cedex, France*
[3]*Max-Born-Institut, Max-Born-Straße 2A, 12489 Berlin, Germany*
[4]*Fachbereich Physik, Freie Universität Berlin, Arnimallee 14, 14195 Berlin, Germany*
[5]*Chemical Sciences and Engineering Division, Argonne National Laboratory, Lemont, Illinois 60439, USA*
[6]*European XFEL, Holzkoppel 4, 22869 Schenefeld, Germany*
[7]*Molecular Physics, Fritz-Haber-Institut der Max-Planck-Gesellschaft, Faradayweg 4-6, 14195 Berlin, Germany*
[8]*Center for Free-Electron Laser Science CFEL, Deutsches Elektronen-Synchrotron DESY, Notkestraße 85, 22607 Hamburg, Germany*
[9]*Department of Physics and James Franck Institute, The University of Chicago, Chicago, Illinois 60637, USA*
[10]*Department of Physics, University of Hamburg, Luruper Chaussee 149, 22761 Hamburg, Germany*
[11]*Department of Physics and Astronomy, University of Turku, 20014 Turku, Finland*
[12]*International Research Laboratory EuXFEL-CNRS, Holzkoppel 4, 22869 Schenefeld, Germany*

(Received 8 May 2026; accepted 2 October 2026; published 4 November 2026)

Double-core-hole (DCH) states offer a unique window into electron correlation and multielectron dynamics. Using intense x-ray free-electron laser (XFEL) pulses and high photon-energy resolution, we generate DCH states in neon via sequential absorption of two x-ray photons within the 1*s* core-hole lifetime (≅2.4 fs). These DCH states are populated, depending on the photon energy, via two different pathways, and they are detected via their KLL hypersatellite Auger decay. A high-photon-energy-resolution study of these two pathways, previously identified in water, allows us to reveal further details of the corresponding processes. The sequential double-ionization with two photons also allows us to study postcollision interaction (PCI) in a four-particle system consisting of the remaining ion, as well as two photoelectrons and one Auger electron, each with well-defined velocities. The observed PCI shift is well described by a theoretical approach based on the eikonal approximation and shows that the influence on the Auger electron is dominated by the slow photoelectron, while the fast photoelectron provides only a minor correction. Calculations show that for the utilized two-photon double-ionization scheme to prepare DCH states, the length of the FEL pulse influences the PCI shift.

DOI: 10.1103/62xn-rkzr

I. INTRODUCTION

Ultrafast electron dynamics in matter can be studied using x-ray photoelectron spectroscopy with intense light sources such as synchrotrons and x-ray free-electron lasers (XFELs). Core-level excitations to highly excited states below the corresponding ionization threshold, followed by ultrafast relaxation processes occurring for light elements on the femtosecond and for heavy elements on the subfemtosecond timescales [1], reveal information about electron correlation and many-body interactions [1–7]. Such processes provide insights into electron and nuclear dynamics in atoms and molecules.

Electron decay dynamics become faster and more sensitive to the chemical environment when double-core-hole (DCH) states are involved [8–10], thereby shortening the timescale even for light elements into the subfemtosecond domain. This allows the study of ultrafast nuclear dynamics on ultrashort timescales, as shown for gas-phase H_2O [4,7] and liquid water [11].

Moreover, DCH states are more sensitive to the chemical environment than single-core-hole (SCH) states [12]. In particular, comparing the ionization potentials of SCH and DCH states allows one to distinguish initial- and final-state effects contributing to the chemical shift [13].

K-shell DCH states can generally be distinguished into three types, namely, (1) doubly ionized K^{-2} states, (2) singly ionized $K^{-2}V$, and (3) neutral $K^{-2}VV'$ DCH states. Strictly speaking, K^{-2}, $K^{-2}V$, and $K^{-2}VV'$ are not states but configurations, since a state is defined by the principal quantum number N, the orbital angular momentum L, the total angular

*Contact author: john.bozek@synchrotron-soleil.fr
†Contact author: marc.simon@sorbonne-universite.fr

Published by the American Physical Society under the terms of the Creative Commons Attribution 4.0 International license. Further distribution of this work must maintain attribution to the author(s) and the published article's title, journal citation, and DOI. Open access publication funded by Max Planck Society.

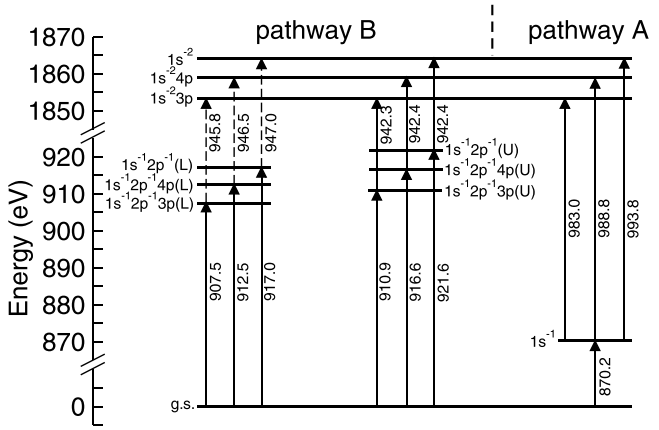


FIG. 1. Energy-level diagram for the states involved in pathway A (right part) and pathway B (left and middle part). The states are labeled next to the horizontal lines, where g.s. represents the electronic ground state. The corresponding transition energies are given beside the arrows. Note that for both pathways, the first step is not resonant, as excess energy is carried away by the photoelectron (not shown), but the second step is, with the exception of the formation of $1s^{-2}$ states via pathway A, and the given transition energies should correspond to the photon energies shown in Fig. 2.

momentum J, and the magnetic quantum number M_J [14]. Nevertheless, we will use the colloquial term "double-core-hole state," which is regularly found in the literature (see, e.g., Refs. [2,15,16]). For the latter two types of states, $K^{-2}V$ and $K^{-2}VV'$, one or two $1s$ electrons are promoted into a virtual orbital, i.e., an orbital unoccupied in the ground state, V (V′). The first two types of DCH states can also be populated starting from the ground state by a single photon via shakeup or shakeoff processes. They can be observed either by electron-electron coincidence [17,18] or indirectly via hypersatellite Auger decay [1]. In addition, the $K^{-2}V$ states can also be obtained by conventional photoelectron spectroscopy [1]. In this case, different DCH states are produced at a given photon energy; i.e., selective population of a single K^{-2} or $K^{-2}V$ DCH state by changing the photon energy is not possible, since the formation process involves electron correlation. The same holds for formation via electron or ion impact. In contrast, selective formation of DCH states starting from the ground state requires a sequential two-photon process, which occurs within the lifetime of an SCH [5,9,19,20]. Such processes do not require strong correlation effects but require extremely high photon fluxes, which are provided only by ultrashort, high-intensity pulses from XFEL sources.

In a recent publication, Ismail *et al.* [9] showed that the population of DCH states with two photons occurs via two different pathways, which are shown in Fig. 1. In the first pathway (pathway A), the first photon ionizes the atom or molecule, leading to a $1s^{-1}$ state. The second photon promotes the remaining $1s$ electron into a virtual orbital ($K^{-2}V$ state) or into the continuum (K^{-2} state), and the entire process can be described by

$$\begin{aligned} \mathrm{Ne} &\xrightarrow{h\nu} \mathrm{Ne}^{1+}(1s^{-1}) + e_{\mathrm{ph1}} \\ &\xrightarrow{h\nu} \mathrm{Ne}^{1+}(1s^{-2}np) + e_{\mathrm{ph1}} \end{aligned}$$

and

$$\begin{aligned} \mathrm{Ne} &\xrightarrow{h\nu} \mathrm{Ne}^{1+}(1s^{-1}) + e_{\mathrm{ph1}} \\ &\xrightarrow{h\nu} \mathrm{Ne}^{2+}(1s^{-2}) + e_{\mathrm{ph1}} + e_{\mathrm{ph2}}, \end{aligned}$$

respectively. Here, e_{ph1} and e_{ph2} are the photoelectrons emitted by the first and second photons, respectively.

In the second pathway (pathway B), core $1s$ ionization by the first photon is accompanied by a shake process in the valence region, leading, in the case of neon, to $1s^{-1}2p^{-1}(n,\epsilon)p$ final states, where n denotes the bound Rydberg states and ϵ denotes the continuum states. The second photon promotes the remaining $1s$ electron into the vacancy in the $2p$ shell. Note that the dipole matrix element for the $1s \rightarrow 2p$ transition is much stronger than that for the $1s \rightarrow np$ transitions with $n \geqslant 3$ and compensates for the lower density of the $1s^{-1}2p^{-1}(n,\epsilon)p$ final states produced by the ionization process with the first photon compared to the $1s^{-1}$ state [9]. The formation of the $K^{-2}V$ states can be described by

$$\begin{aligned} \mathrm{Ne} &\xrightarrow{h\nu} \mathrm{Ne}^{1+}(1s^{-1}2p^{-1}np) + e_{\mathrm{ph1}} \\ &\xrightarrow{h\nu} \mathrm{Ne}^{2+}(1s^{-2}np) + e_{\mathrm{ph1}} \end{aligned}$$

and of the K^{-2} states by

$$\begin{aligned} \mathrm{Ne} &\xrightarrow{h\nu} \mathrm{Ne}^{2+}(1s^{-1}2p^{-1}) + e_{\mathrm{ph1}} + e_{\mathrm{ph2}} \\ &\xrightarrow{h\nu} \mathrm{Ne}^{2+}(1s^{-2}) + e_{\mathrm{ph1}} + e_{\mathrm{ph2}}. \end{aligned}$$

In pathway B, the absorption of the second photon leads to a resonant $1s \rightarrow 2p$ excitation that repopulates the $2p$ hole. Because of this, the spectral features of pathway B are generally found at lower photon energies, as can be seen from the energies given in Fig. 1 and the upper panel of Fig. 2, which shows an integration of the map displayed in the lower panel along the electron-energy axis and represents an absorption spectrum for the second photon. Moreover, the $K^{-2}V$ and the K^{-2} DCH states populated via pathway A are visible at different photon energies, while the $K^{-2}V$ and the K^{-2} DCH states populated via pathway B are excited with almost identical photon energies. Because of this, pathway A allows $K^{-2}V$ and K^{-2} DCH states to be prepared selectively using a narrow-band, one-color two-photon scheme; this scheme is used in the present work. The population of $K^{-2}VV'$ DCH states requires either a broadband one-color or a narrow-band two-color two-photon scheme. Note that a broadband one-color scheme has been used by Pelimanni *et al.* [21] to populate $K^{-1}K^{-1}V^2$ two-site DCH states of N_2.

In this work, we produce both $K^{-2}V$ and K^{-2} states via both pathways A and B. Since the $K^{-2}V$ states of neon populated via pathway A are already extensively studied [5,20,22], we focus in the present work on differences between pathways A and B, details on pathway B, and the postcollision interaction (PCI) effect of K^{-2} states produced by pathway A. The high photon-energy resolution used in the present work and the simplicity of the neon atom as compared to the water molecule studied previously [9] allow us to reveal additional details on both pathways.

The PCI effect, which is studied in the present work using the Auger spectra of the K^{-2} states of neon, is generally a

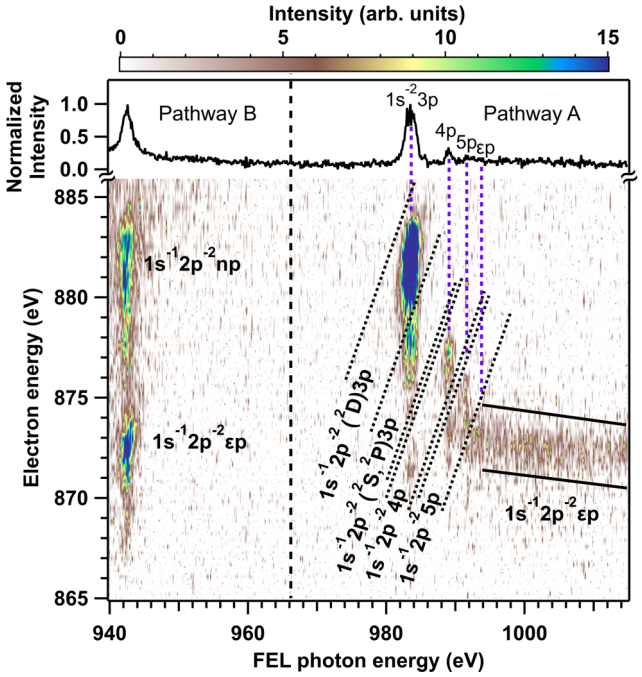


FIG. 2. Lower panel: 2D map of the intensity of electron emission in the Auger hypersatellite region of double-core holes in neon over a photon-energy range around the second K-shell threshold at 993.8 eV. The data were measured in the vertical direction to effectively suppress background caused by the 2*s* valence ionization. The intensities are given by a linear color code shown above the map, and the final states of the Auger decay are labeled next to the corresponding spectral features. Upper panel: Integration along the electron energy dimension of the 2D map representing an absorption signal for the second photon. In this panel, for pathway A, the energy positions of $1s^{-2}(n,\epsilon)p$ DCH states are indicated.

well-known effect due to the interaction of a slow photoelectron and a fast Auger electron in the field of the ion, and can in the case of a single ionization be understood as a three-body energy exchange mechanism [23,24]. The effect leads to an energy shift and a line distortion of photoelectron and Auger lines and has been extensively studied for single-core ionization [24–28], but remains largely unexplored for DCH states, where two photoelectrons are emitted so that the PCI effect becomes a four-body energy-exchange mechanism. Three synchrotron-based studies in neon and argon [1,29,30] revealed in the Auger spectra partial PCI signatures of DCH states, but could not capture key features such as PCI-induced energy shifts or photoelectron recapture. The difficulty arises from the one-photon process used in Refs. [1,29,30] to form the DCHs, which generates two photoelectrons of unknown individual kinetic energy. The energy sharing normally leads to one slow and one fast electron [18]; however, the kinetic energies of the individual photoelectrons cannot be resolved without electron-electron coincidence spectroscopy. Moreover, in a one-photon process, the kinetic energies of the photoelectrons cannot be changed in a controlled way. As a result, it is difficult to identify which of the two photoelectrons interacts more strongly with the Auger electron and causes the PCI effect. This problem can be solved by the production of the K^{-2} states via pathway A, since in this way photoelectrons with variable but well-defined kinetic energies can be prepared. This allows us to study the four-body problem in more detail using well-defined photon energies for the electrons involved.

In summary, we use two-photon absorption processes to populate K^{-2} and $K^{-2}V$ DCH states in neon and aim to elucidate PCI mechanisms in four-particle systems as well as to compare pathways A and B for DCH formation. For the latter aspect, we also address differences between atoms and molecules.

II. EXPERIMENT

The measurements were performed at the small quantum systems (SQS) instrument of the European x-ray free-electron laser (EuXFEL) [31], which is dedicated to investigating fundamental processes of light-matter interaction in the soft x-ray regime. The self-amplified spontaneous emission (SASE3) undulator beamline of the EuXFEL [32], equipped with variable polarization capability, provides intense, ultrashort x-ray pulses in the 250–3000 eV photon-energy range. In the present experiment, we employed linearly polarized radiation in the horizontal plane.

For the present study, the photon energy was scanned over a range of 940–1015 eV in 0.1 eV steps. The pulses with a duration of ≈25 fs and an energy of 7.5 mJ were delivered with an effective pulse-train repetition rate of up to 3.5 kHz. The x-ray beam was focused to a spot size of 1.5×1.5 μm^2 using Kirkpatrick-Baez mirrors [33] at a grazing-incidence angle of 9 mrad relative to the experimental chamber.

The photon beam was monochromatized with a variable line-spacing grating monochromator, equipped with gratings of 150 lines/mm and 50 lines/mm [34]. Using the 50 lines/mm grating with 400 μm exit slit provided an estimated photon bandwidth of ≈1.3 eV [34], which is slightly larger than the result of 1.0 ± 0.1 eV obtained from a fit analysis of spectral features present in Fig. 2. Transmission through the monochromator stretched the pulses to ≈30 fs [34] and yielded photon flux corresponding to an energy of 35 μJ, which corresponds to a peak intensity of 5.7×10^{16} W cm^{-2}. During the experiment, Neon was injected effusively through a 100 μm inner-diameter nozzle, resulting in a chamber pressure of about 3×10^{-8} mbar under gas load.

The DCH states of neon were studied by detecting KLL hypersatellite Auger electrons. The electrons were collected with high-resolution electron time-of-flight (eTOF) spectrometers [35] arranged at three detection angles with respect to the XFEL polarization: vertical (90°), horizontal (0°), and magic angle (54.7°). The presented data were recorded with the eTOF mounted in the vertical direction, since the spectra recorded in the other two directions show significant background caused by the 2*s* valence-ionization lines, both the main line and the satellites, due to their angular distribution. Note that at photon energies around 1000 eV, the 2*s* photoionization cross section is significantly larger than the 2*p* ionization cross section. For the data analysis of the PCI effect, the data recorded in the horizontal direction were used, since they show a high count rate and, therefore, less noise above the DCH ionization threshold. The spectrometers were aligned relative to the intersection of the XFEL beam and

the gas jet by maximizing the signal from a reference Ne KLL Auger line. Each eTOF spectrometer is equipped with multielement electrostatic lenses. This lens system enables the application of retardation or acceleration voltages to optimize either the kinetic-energy resolution or the electron acceptance. In the present experiment, a retardation potential of 825 V was applied, yielding an estimated kinetic-energy resolution of ≈350 meV.

Complementary PCI studies on Ne $1s^{-1}$ SCH photoemission were performed at the PLEIADES beamline of the SOLEIL synchrotron facility [36]. This beamline is equipped with an APPLE II HU80 permanent-magnet undulator, providing linearly polarized radiation in the soft x-ray range. The photon beam was monochromatized using a 600 lines/mm grating, yielding a photon bandwidth of ≈120 meV at the Ne $1s^{-1}$ ionization threshold. The experiments were conducted at a permanent gas-phase electron spectroscopy endstation. The gas pressure in the chamber was maintained at 1×10^{-5} mbar. Ne $1s$ photoelectrons were recorded with a VG Scienta R4000 hemispherical analyzer operated at 5 eV pass energy with a 0.2 mm curved entrance slit to measure the very slow electrons. Due to the low pass energy necessary for the detection of slow photoelectrons and the small entrance slit, the analyzer resolution is very high and can be neglected compared to the total experimental resolution equal to the photon bandwidth of ≈120 meV. Photon energies between 872 and 900 eV were used, producing photoelectrons with excess energies up to 30 eV.

III. RESULTS AND DISCUSSION

A. Overview

Figure 2 shows the two-dimensional (2D) map of hypersatellite Auger electron intensities of neon DCH states created by sequential absorption of two photons. In the map, the x axis represents the photon energy and the y axis the kinetic energy of the Auger electrons. The electron spectra were recorded with the eTOF spectrometers in the kinetic-energy range 865–886 eV, while the photon energy was scanned from 940 to 1015 eV in 0.1 eV steps to cover the relevant excitation and ionization channels. This map, therefore, provides a global view of all electronic processes leading to hypersatellite Auger emission following DCH formation by the intense XFEL pulses.

As explained above, the upper panel of Fig. 2 represents an absorption spectrum for the second photon. For pathway A, several peaks are observed in the energy range from 982 to 994 eV and assigned to $1s^{-2}np$ states. In contrast, for pathway B, only one peak at 943 eV is found, which can be assigned to different overlapping excitations; for details, see below. These overlapping excitations readily explain the different Auger structures for the two pathways, since the decay is independent of the formation pathway. For $K^{-2}V$ DCH states, it is given by

$$Ne^{1+}(1s^{-2}np) \rightarrow Ne^{2+}(1s^{-1}2p^{-2}mp) + e_{\text{Auger}},$$

with e_{Auger} being the Auger electron. Auger transitions with $m = n$ describe spectator decays, while those with $m \neq n$ describe participator Auger decays due to shake processes. The K^{-2} DCH states decay via

$$Ne^{2+}(1s^{-2}) \rightarrow Ne^{3+}(1s^{-1}2p^{-2}) + e_{\text{Auger}}.$$

We shall first briefly discuss the $K^{-2}V$ DCH states populated via pathway A, followed by the $K^{-2}V$ and K^{-2} DCH states populated via pathway B, and finally the K^{-2} DCH states populated via pathway A, where we focus on the PCI effect. We also compare the spectral features formed by the two pathways.

B. $K^{-2}V$ DCH states via pathway A

The spectral features caused by pathway A are visible at photon energies above 980 eV and can be found in Fig. 2 on the right side of the vertical dashed line. We shall now focus on the resonantly excited $K^{-2}V$ DCH states, which are found in the photon-energy range of 980–993.8 eV, while above the latter value the doubly ionized K^{-2} state is populated. The photon energies required for the excitations to the $1s^{-2}np$ states and the ionization threshold $1s^{-2}\epsilon p$ are indicated in the upper panel of Fig. 2. The different final states of the hypersatellite Auger decay are shown along the dashed diagonal lines and are also labeled in Fig. 2.

The structures of the $K^{-2}V$ DCH were previously observed and discussed in Ref. [5] using the SASE beam with a photon bandwidth of about 8.5 eV, as well as in Ref. [20] using a monochromatic beam with a photon bandwidth of about 430 meV, i.e., with a resolution better than in the present case, which allows them to resolve the resonance structures in pathway A in much greater detail. Moreover, these spectral features are discussed theoretically by Kiselev *et al.* [22], so we do not give a detailed discussion on the assignment of these spectral features. In short, the assignment of the spectral features is given by the labels in Fig. 2.

Note that the spectral features are due to a resonant Auger process, so that the final states generally follow a linear dispersion as indicated by the diagonal lines. This can be seen, e.g., for the hypersatellite Auger decay to the $1s^{-1}2p^{-4}4p$ final-state configuration, which can be found as a shakeup satellite of the $1s^{-2}3p$ state at a kinetic energy of ≈871.5 eV and as spectator decay of the $1s^{-2}4p$ state at ≈877 eV.

In contrast to such a linear dispersion, the individual islands in the 2D map predominantly exhibit a vertical orientation. Nevertheless, a detailed analysis of the most intense (dark blue) island at photon energies of 983.5 eV and kinetic energies around 882 eV representing the $1s^{-2}3p \rightarrow 1s^{-1}2p^{-2}3p$ hypersatellite Auger transitions is not strictly vertical. Instead, a fit analysis reveals that the high-kinetic energy part of this island is located about 300 meV higher in photon energy than the low-kinetic energy part.

There are two reasons for this complex behavior. First, each island shows different transitions with slightly different kinetic energies since each $1s^{-1}2p^{-4}np$ final-state configuration leads to various final states (see Kiselev *et al.* [22]); this results in a stretching of the islands in the vertical direction. Second, as discussed by Gel'mukhanov and Ågren [37] as well as Kukk *et al.* [38], the exact dispersion of resonant Auger transitions in 2D maps depends on the combination of lifetime broadening and experimental resolutions. For experiments performed in resonant-Raman conditions, i.e., with

an experimental resolution much smaller than the lifetime broadening, the dispersion is linear with a slope of 1. In the experiments by Mazza *et al.* [20], these conditions are fulfilled. For the case of an experimental resolution large compared to the lifetime width, the dispersion is expected to be strictly vertical. In the present case, however, the resolution of about 1.0 eV is only slightly larger than the DCH lifetime of 700 meV, which leads to a more complex behavior, namely, to a vertical dispersion close to the resonance energy, which turns back to a linear behavior further away from it resulting in an S-shape behavior [37,38], in agreement with the observation.

C. DCH states via pathway B

At photon energies around 943 eV, a second set of hypersatellite Auger structures is observed and assigned in accordance with Ref. [9] to pathway B. To interpret these features around 943 eV in detail, we compare the observed resonances with known excitation energies from the literature, summarized by the energy-level diagram in Fig. 1. The relevant states belong to the configurations $1s^{-1}2p^{-1}np$, $1s^{-1}2p^{-1}$, $1s^{-2}np$, and $1s^{-2}$, and their energies are referenced relative to the ground state (g.s.). Reported data place the SCH shakeup satellites in the 907.5–921.6 eV range above the ground state [39,40] and the DCH states in the 1853.3–1864.0 eV range [1].

The final states of the intermediate configuration $1s^{-1}2p^{-1}np$ separate into two Rydberg series, namely, $1s^{-1}2p^{-1}np(L)$ and $1s^{-1}2p^{-1}np(U)$, which converge toward the thresholds $1s^{-1}2p^{-1}(L)$ and $1s^{-1}2p^{-1}(U)$. The levels of the (L) series lie at lower energies, corresponding to states where the $1s^{-1}$ and $2p^{-1}$ couple predominantly to a triplet. Conversely, the (U) series corresponds to singlet-coupled hole states and, therefore, appears at higher energies.

Based on the energy levels summarized in Fig. 1, two series of resonances are expected. The $1s^{-1}2p^{-1}(n,\epsilon)p(U) \rightarrow 1s^{-2}(n,\epsilon)p$ transitions should occur at photon energies around 942.4 eV (vertical solid arrows in the middle of Fig. 1), while the $1s^{-1}2p^{-1}(n,\epsilon)p(L) \rightarrow 1s^{-2}(n,\epsilon)p$ transitions are predicted near 946.5 eV (vertical dashed arrows in the left part of Fig. 2).

In the present study, pronounced structures are experimentally observed around 943 eV in Fig. 2, but no corresponding features appear around 946.5 eV. The absence of the latter series can readily be understood based on dipole selection rules: In the $1s^{-1}2p^{-1}(n,\epsilon)p(L)$ series, the $1s$ and the $2p$ holes couple predominantly to a triplet state. Consequently, the remaining $1s$ electron and the $2p$ vacancy have opposite spin orientation, making the required $1s \rightarrow 2p$ excitation a spin-flip transition, which is strongly suppressed. In contrast, in the states of the (U) series, the spins of the remaining $1s$ electron and the $2p$ electrons couple to a singlet so that the $1s \rightarrow 2p$ excitation is dipole allowed. The $1s^{-1}2p^{-1}np(U) \rightarrow 1s^{-2}np$ transitions at a photon energy of 943 eV agree within the experimental uncertainties with the prediction of 942.4 eV. Finer details of the excitation energies for the observed series will be discussed further below, since this requires a better understanding of the resonant Auger transitions, which shall be given in the following.

In the 2D map, one can observe that the strongest spectral feature for pathway A is the $1s^{-2}3p \rightarrow 1s^{-1}2p^{-2}(^2D)3p$ resonant Auger decay, while for pathway B the $1s^{-2} \rightarrow 1s^{-1}2p^{-2}(^2D)$ normal Auger decay dominates. This can readily be understood based on the population of the DCH states. In pathway A, for all final DCH states, the intermediate SCH state is identical, so that the resonant population of the $1s^{-2}3p$ state is stronger than the nonresonant population of the $1s^{-2}$ continuum (see upper panel of Fig. 2). This finding is in full agreement with the observations in H_2O [9]. In pathway B, the population of the final DCH state is determined by the shake process in the first ionization step since the transition probability of the $1s \rightarrow 2p$ excitation in the second step is rather independent of the initial state. Because of this, the $1s^{-2}3p \rightarrow 1s^{-1}2p^{-2}(^2D)3p$ to $1s^{-2} \rightarrow 1s^{-1}2p^{-2}(^2D)$ intensity ratio of pathway B is determined by the $2p \rightarrow 3p$ shakeup to $2p$ shakeoff ratio of the first ionization step, which can be estimated from the satellite photoelectron spectrum of Svensson *et al.* [39] of the Ne $1s$ ionization. This spectrum clearly shows that the shakeoff process (integrated intensity of the background) is significantly more intense than the $2p \rightarrow 3p$ shakeup process and explains the observation.

The influence of the shakeoff continuum can also be seen in Fig. 3, which shows Auger spectra obtained from the 2D map in Fig. 2 by integrating over selected photon energies to represent selected pathways. In Fig. 3(a), the photon energy is integrated over the energy range from 940 to 945 eV and presents the total hypersatellite Auger spectrum for pathway B. The presented spectrum is obtained by subtracting a linear background caused by two-photon valence double ionization; this process can also be seen in the upper panel of Fig. 2 by the background increasing slowly with decreasing photon energies.

To assign the Auger spectrum of pathway B, panels (c)–(f) show the hypersatellite decays of the $1s^{-2}$ continuum (integration region from 1000 to 1005 eV) populated via pathway A, of the $1s^{-2}5p$ state (integration region from 991 to 992 eV), of the $1s^{-2}4p$ state (integration region from 988 to 991 eV), and of the $1s^{-2}3p$ state (integration region from 980 to 987 eV), respectively. The dotted vertical lines indicate the kinetic-energy positions of the highest intensities in the Auger spectra of the $1s^{-2}n,\epsilon p$ states and allow to assign the spectral features in the Auger spectrum of pathway B [panel (a)]. As discussed above, the dominating feature at a kinetic energy of ≈872.5 eV is caused by the $1s^{-2}\epsilon p \rightarrow 1s^{-1}2p^{-2}\epsilon p$ normal Auger transition and also partially by higher-n $1s^{-2}np \rightarrow 1s^{-1}2p^{-2}np$ ($n \geqslant 5$) resonant Auger transitions while the $1s^{-2}3p \rightarrow 1s^{-1}2p^{-2}3p$ resonant Auger decays around 882 eV are slightly less intense.

Finally, Fig. 3(b) shows the Auger spectrum by integrating over the photon-energy range from 980 to 1015 eV. This spectrum matches quite well that of pathway B presented in Fig. 3(a) and shows that a summation over different DCH initial states has a significant influence on the Auger spectrum. This holds, in particular, of the doubly ionized $1s^{-2}$ DCH states since they are not resonantly excited, but can be populated with a low intensity over a large photon energy range (see upper panel of Fig. 2).

The intensity ratios for the Auger transitions of pathway B observed for neon cannot be confirmed by similar studies

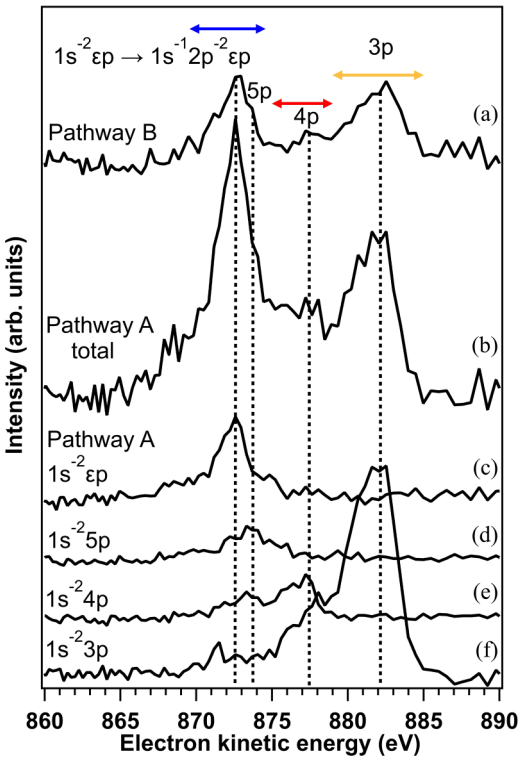


FIG. 3. Auger spectra obtained by integrating over different photon energies in the two-dimensional map shown in Fig. 2. (a) Auger spectrum associated with pathway B. (b) Auger spectrum obtained by integrating over the entire region of pathway A, including the continuum region. (c) Auger spectrum of the dicationic $1s^{-2}$ states populated via pathway A. (d)–(f) Auger spectra associated with the $1s^{-2}5p$, $1s^{-2}4p$, and $1s^{-2}3p$ DCH states populated via pathway A, respectively. For more details, see the text. The colored arrows in the upper part of the figure indicate the range of kinetic energies used to produce the spectra shown in Fig. 4.

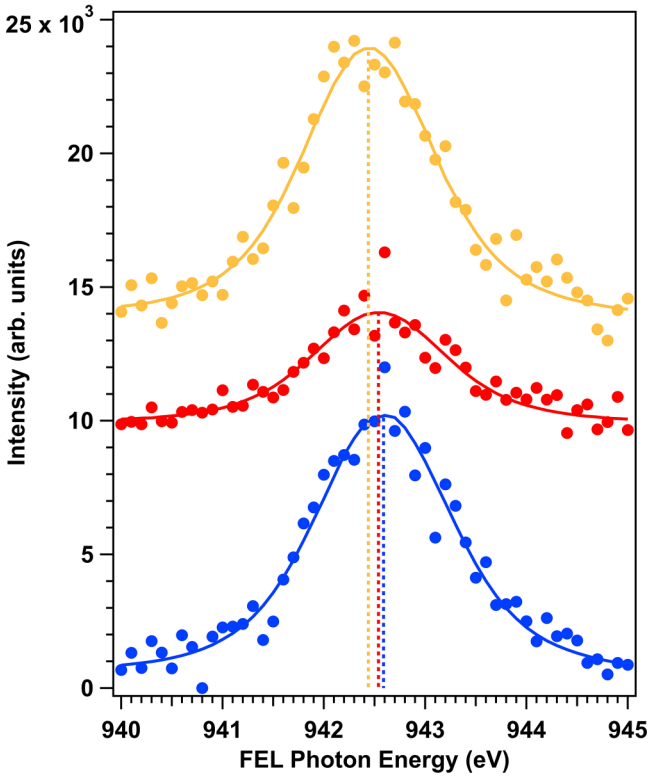


FIG. 4. Spectra representing the absorption signal of the second photon for different $1s^{-1}2p^{-1}(n,\epsilon)p \rightarrow 1s^{-2}(n,\epsilon)p$ transitions. The spectra are obtained by integrating the signal of the 2D map shown in Fig. 2 over selected kinetic-energy regions. The color of the spectra agrees with the colored energy regions shown in the upper part of Fig. 3, i.e., the orange spectrum represents the $1s^{-1}2p^{-1}3p \rightarrow 1s^{-2}3p$ transition, the red one an overlap of the $1s^{-1}2p^{-1}3p \rightarrow 1s^{-2}3p$ and $1s^{-1}2p^{-1}4p \rightarrow 1s^{-2}4p$ transitions, and the blue one the $1s^{-1}2p^{-1}np \rightarrow 1s^{-2}np$ transitions with $n \geqslant 5$ and, in particular, the $1s^{-1}2p^{-1}\epsilon p \rightarrow 1s^{-2}\epsilon p$ transition. The solid-colored lines through the data points are the fitted results, and the colored vertical dashed lines indicate the energy positions of each peak. For more details, see the text.

on water [9] since the corresponding spectral features overlap partially with those of other processes. Moreover, in molecules $\tilde{V} \rightarrow V$ shake transitions within the $2p$ shell are possible, which may significantly change the shakeup to shakeoff ratio. Obviously, for a conclusive answer on this issue, more detailed studies on molecules are necessary.

Finally, we shall return to the excitation energies for the observed pathway B via the $1s^{-1}2p^{-1}(n,\epsilon)p(U) \rightarrow 1s^{-2}(n,\epsilon)p$ transitions. The calculated values given in Fig. 1 show a small increase with n in the order of 0.1 eV. To prove this experimentally, we show in Fig. 4 spectra along the photon energy axis, which are obtained by integrating over different kinetic-energy regions indicated by the colored arrows in Fig. 3. The orange spectrum is obtained by an integration over a kinetic-energy region where only Auger decays of the $1s^{-2}3p$ DCH state contribute. The red spectrum shows contributions of the $1s^{-2}3p$ and $1s^{-2}4p$ DCH states. The blue spectrum is dominated by the decay of the doubly ionized $1s^{-2}$ DCH state. These three spectra are fitted with a Voigt profile. In detail, a fixed Lorentzian linewidth of 960 meV, accounting for the lifetime broadening of the SCH initial state and the DCH final state, is convoluted with a Gaussian profile with the width as a free parameter, resulting in a value of 1.0 ± 0.1 eV. The obtained peak position for the $1s^{-1}3p \rightarrow 1s^{-2}3p$ transition (orange spectrum) is 942.44 ± 0.03 eV and that for the $1s^{-1} \rightarrow 1s^{-2}$ transition (blue spectrum) 942.59 ± 0.04 eV. The difference of 0.15 ± 0.05 eV agrees well with the calculated value of 0.1 eV given in Fig. 1. Note that no accurate calibration for the absolute photon energies is performed.

The red spectrum with contributions from the $1s^{-1}3p \rightarrow 1s^{-2}3p$ and $1s^{-1}4p \rightarrow 1s^{-2}4p$ transitions shows a peak maximum at 942.45 ± 0.05 eV, indicating that the latter transition requires a slightly higher photon energy than the former one. The individual energy for the $1s^{-1}4p \rightarrow 1s^{-2}4p$ transition could, however, not be derived due to insufficient statistics.

Note that the almost equal resonance energies for pathway B arise because of the fact that the shaken $(n,\epsilon)p$ electron has, as a spectator of the process, almost no influence on the $1s \rightarrow 2p$ excitation energy. This is, however, a specific characteristic of the closed-shell neon atom. As can be seen in Ref. [9] (Fig. 3), the excitations of pathway B in H_2O spread

over almost 10 eV. This difference can readily be explained by two facts. First, in water, the shake process can start from different occupied O $2p$-derived valence orbitals $\tilde{V} = 1b_2$, $3a_1$, and $1b_1$ so that different orbitals can be populated in the second step. Second, in water, the virtual orbitals V can also be of O $2p$-derived character. In this case, there is a large spatial overlap of $\tilde{V}$ and V so that the population of different virtual orbitals V leads to different screening effects of the orbitals $\tilde{V}$ and, as a consequence, to different excitation energies in the second step. In contrast, in neon, $\tilde{V} = 2p$ and $V = np$, with $n \geqslant 3$, i.e., the spatial overlap between $\tilde{V}$ and V is small.

D. K^{-2} DCH states via pathway A: PCI analysis

K^{-2} DCH states are produced by the sequential absorption of two identical photons when the photon energy is tuned above the Ne $1s^{-1}$ threshold of K-shell-ionized Ne^+ at ≈993.8 eV. As described above, these states decay predominantly via $1s^{-2} \rightarrow 1s^{-1}2p^{-2}$ KLL hypersatellite Auger decay, with $1s^{-2} \rightarrow 1s^{-1}[2p^{-2}(^1D_2)](^2D_{3/2;5/2})$ being the most intense transition; without PCI shift, this transition is located at a kinetic energy of 870.54 eV [1]. In the course of the excitation and decay process, three electrons are produced, namely, a fast Auger electron, e_{Auger}, a medium-velocity first photoelectron, e_{ph1}, and a slow second photoelectron, e_{ph2}. Here, in particular, the Coulomb interaction between the slow photoelectron and the fast Auger electron leads to PCI, manifesting as a characteristic shift of the Auger line to higher kinetic energies. This effect is visible in Fig. 2 between photon energies of 993.8 and 1015 eV, where the Auger feature bends with increasing photon energy. The PCI effect becomes more obvious after a detailed data analysis, as presented in Fig. 6.

In detail, the first photon produces a photoelectron with kinetic energy $E_{KE1} = h\nu - IP_1$, with $IP_1 = 870.2$ eV being the $1s$ ionization energy of neutral neon. In the photon-energy region of 993.8 to about 1015 eV used for the PCI studies, this photoelectron possesses kinetic energies between 123.6 and about 144 eV. The subsequent second photon promotes the second photoelectron with $E_{KE2} = h\nu - IP_2$ into the continuum. Here, $IP_2 = IP_1 + 123.6\,\text{eV} = 993.8$ eV is the increased binding energy of the second $1s$ electron due to the presence of the initial core vacancy [22,41], leading to kinetic energies between 0 and 20 eV for the second photoelectron.

The Auger electron leaves the neon ion with an average time delay of ≈0.95 fs relative to the photoelectron e_{ph2}, corresponding to the DCH lifetime associated with a linewidth of $\Gamma_{\text{DCH}} = 0.700\,\text{eV}$ [1]. However, due to the much higher kinetic energy, it overtakes e_{ph2} after a relatively short time. Because of this, the slow photoelectron experiences a sudden change in the ionic field as the effective ion charge state changes from doubly to triply charged, while the fast Auger electron experiences a change in the ionic field from triply to doubly charged. As a result, the photoelectron loses kinetic energy ΔE_2, while the Auger electron gains this energy. A similar energy exchange ΔE_1 occurs at a later time when the Auger electron overtakes the faster photoelectron e_{ph1}. This redistribution of kinetic energy also manifests as an asymmetric line shape: Photoelectron spectra are broadened with tails toward lower kinetic energies, while Auger electron spectra exhibit tails on the higher-kinetic-energy side. This characteristic distortion is referred to as PCI tailing.

The main difference between the interaction of the Auger electron with the two photoelectrons is the time delay. In the case of the interaction with e_{ph2}, the time delay is determined by the DCH lifetime, while for the interaction with e_{ph1}, the time delay between the absorption of the two photons also plays a role. The exact time delay is unknown; however, for efficient production of DCH states, it should lie between zero and the SCH lifetime of about 2.4 fs [42]. It is, however, clear that the PCI effect on the Auger electron is maximal if the time delay between the absorption of the two photons is zero. This limiting case allows us to estimate an upper limit for the influence of e_{ph1}.

The PCI shift for an isolated atom can be quantitatively described using a theoretical model based on the eikonal approximation [23,26,43]. The model provides an analytical expression for the PCI-induced energy shift by accounting for the sudden change in the Coulomb potential experienced by the electrons [26]. For a single photoelectron and an Auger electron, the PCI shift can be written as [26,28,43]

$$\Delta E = C\frac{e^2}{4\pi\epsilon_0\hbar}\frac{\Gamma_A}{2}\left(\frac{1}{v_{\text{ph}}} - \frac{1}{|\vec{v}_A - \vec{v}_{\text{ph}}|}\right), \tag{1}$$

where $\vec{v}_{\text{ph}}$ and $\vec{v}_A$ are the velocities of the photoelectron and the Auger electron, respectively, and v_{ph} is the norm of $\vec{v}_{\text{ph}}$. The constants e, ϵ_0, and $\hbar$ represent the elementary electric charge, the vacuum permittivity, and the reduced Planck constant, respectively. By default, all quantities are given in SI units. The constant C describes the direction of the PCI shift and is equal to $+1$ for Auger electrons and -1 for photoelectrons.

However, this PCI estimation changes when considering two photoelectrons and one Auger electron. For Ar $2p$ core-valence double ionization by one photon, i.e., by simultaneous emission of both photoelectrons, Huttula *et al.* developed and applied the equation [29]

$$\Delta E' = \Delta E_1 + \Delta E_2, \tag{2}$$

with

$$\Delta E_{1,2} = C\frac{e^2}{4\pi\epsilon_0\hbar}\frac{\Gamma_A}{2}\left(\frac{1}{v_{\text{ph }1,2}} - \frac{1}{|\vec{v}_A - \vec{v}_{\text{ph }1,2}|}\right) \tag{3}$$

where $\vec{v}_{\text{ph1}}$ and $\vec{v}_{\text{ph2}}$ are the velocities of the first photoelectron e_{ph1} and the second photoelectron e_{ph2}, respectively. Under the present experimental conditions, with the Auger electron being much faster than the photoelectrons, the terms $e^2/|\vec{v}_A - \vec{v}_{\text{ph1}}|$ and $e^2/|\vec{v}_A - \vec{v}_{\text{ph2}}|$ are negligible compared to e^2/v_{ph1} and e^2/v_{ph2} and are therefore omitted in the subsequent discussion. This approximation makes the PCI shift independent of the emission direction of the photoelectrons. As we will show in detail in the Appendix, this allows us to simplify the PCI shifts to

$$\Delta E_{1,2} \approx C\,\frac{\Gamma_A}{2} \times \sqrt{\frac{13.6}{E_{\text{ph }i}[\text{eV}]}}, \tag{4}$$

where $E_{\text{ph }i}[\text{eV}]$ is the kinetic energy of electron i given in eV.

Here, we apply this formalism to describe the PCI shift in the neon hypersatellite Auger spectra following creation

of a DCH, taking $\Gamma_A = \Gamma_{\rm DCH} = 0.700\,{\rm eV}$ [1] for the DCH lifetime. The fact that the formula is developed for double ionization with one photon implies that the two electrons are emitted simultaneously, which is the case for a two-photon process only if both photons are absorbed at the same time. As discussed above, a zero time delay therefore represents an upper limit for the total PCI shift within the given model. It is, however, well suited for experiments performed with x-ray pulses much shorter than the core-hole lifetime.

In the next step, we take the time delay between the absorption of the first and the second photon into account. For this, we can use a model developed for the second-step Auger decay subsequent to x-ray emission [3,44], using an effective lifetime since, in the present experiment, the pulse length of the x-ray source is long compared to the core-hole lifetime of the SCH. For this, we will first explain the model for the case of Ar 1*s* ionization described by Guillemin *et al.* [3], namely, the process

$$\begin{aligned} {\rm Ar} &\xrightarrow{h\nu} {\rm Ar}^{1+}(1s^{-1}) + e_{\rm ph1} \\ &\rightarrow {\rm Ar}^{1+}(2p^{-1}) + e_{\rm ph1} + \gamma \\ &\rightarrow {\rm Ar}^{2+}(3p^{-2}) + e_{\rm ph1} + \gamma + e_{\rm Auger}. \end{aligned}$$

Here, the first line describes the emission of a photoelectron, the second line an x-ray emission decay, and finally the third line the Auger decay of the $2p^{-1}$ core hole. In this case, the PCI effect can be described using an effective core-hole lifetime broadening $\Gamma_{\rm eff} = \Gamma_{1s}\Gamma_{2p}/(\Gamma_{1s} + \Gamma_{2p})$, which takes into account that the emission of the Auger electron is delayed by the 1*s* core-hole lifetime due to the intermediate step of the emission of the x-ray photon.

To describe the present process,

$$\begin{aligned} {\rm Ne} &\xrightarrow{h\nu} {\rm Ne}^{1+}(1s^{-1}) + e_{\rm ph1} \\ &\xrightarrow{h\nu} {\rm Ne}^{2+}(1s^{-2}) + e_{\rm ph1} + e_{\rm ph2} \\ &\rightarrow {\rm Ne}^{3+}(1s^{-1}2p^{-2}) + e_{\rm ph1} + e_{\rm ph2} + e_{\rm Auger}, \end{aligned}$$

we can use the same approach for reasons that shall be discussed in the following. In detail, we replace in the second step the x-ray emission process with an x-ray absorption process. In both cases, the probability of the process is proportional to the population of the initial core-hole state, so that a constant photon flux in the absorption process should lead to an identical temporal dependence, which is given by the lifetime of the initial core hole. Note that the constant photon flux can be assumed since the present pulse duration of ≈30 fs is long compared to the Ne 1*s* core-hole lifetime of 2.4 fs. The emission of a very slow second photoelectron does not have a direct influence on the much faster first photoelectron since the latter always sees a charge of +1 until it is overtaken by the fast Auger electron; a possible small increase in kinetic energy of the Auger electron due to the PCI effect with the second photoelectron can safely be neglected. Within this approach in Eq. (2), the PCI shift for the first photoelectron can be written as

$$\Delta E_1 = C\frac{e^2}{4\pi\epsilon_0\hbar}\frac{\Gamma_{\rm eff}}{2}\left(\frac{1}{v_{\rm ph1}} - \frac{1}{|\vec{v}_A - \vec{v}_{\rm ph1}|}\right). \qquad (5)$$

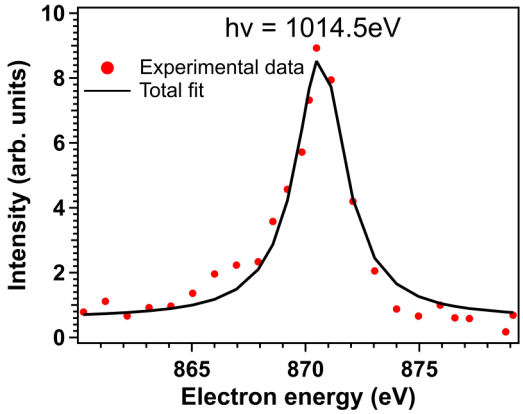


FIG. 5. Fit of the most intense main feature of the hypersatellite Auger line $1s^{-2} \rightarrow 1s^{-1}[2p^{-2}(^1D_2)](^2D)$, recorded at $h\nu = 1014.5\,{\rm eV}$ and shown here as an example of the recorded spectra. Note that this spectrum was recorded in the horizontal direction due to the higher efficiency of the corresponding eTOF.

All PCI approaches discussed above are based on the eikonal approximation and do not consider effects relevant at short distances, such as incomplete screening of the nuclear charge and scattering due to multiple decay pathways. Because of this, Eqs. (1) and (2) are applicable only if the photoelectron energy is much higher than the PCI shift [26,28]. This is considered to be valid for $E_{\rm ph} > E_0 = \Gamma_A^{2/3}(E_H/2)^{1/3}$ [28,43], with E_H being 1 hartree or ≈27.21 eV. For the DCH states of neon, $E_0 = 1.9\,{\rm eV}$.

In the following, we shall analyze the PCI shifts of Auger spectra measured above the Ne $1s^{-2}$ edge. Since the count rates for the Ne DCH KLL Auger electrons are very low and the background is high, resulting in a poor signal-to-noise ratio, we first added 10 spectra recorded with a 0.1 eV photon-energy step width into one spectrum. The resulting spectrum was fitted with a Voigt function to determine the exact peak position (see Fig. 5).

The obtained PCI shifts as a function of the excess energy are presented in blue in Fig. 6. This PCI shift is also directly visible in the 2D map (see Fig. 2) and is indicated above 994 eV by two diagonal lines with a slight negative slope. For comparison, the PCI shifts for Ne $1s^{-1}$ photoelectron spectra recorded at the PLEIADES beamline of the synchrotron radiation facility SOLEIL are shown in purple dots. Note that the PCI shifts for the photoelectron and the corresponding Auger spectra are equal in size but opposite in direction (see above). As expected, the PCI shifts decrease with increasing excess photon energy. Obviously, the PCI shifts for the DCH states are significantly larger than those for the SCH states, which can be understood based on Eqs. (1) and (2) in combination with the much larger lifetime width of the former states of 700 meV [1] as compared to the latter states of 270 meV [42].

In the next step, we shall compare the experimental results with the prediction of the eikonal approximation. The red solid curve represents the results for the SCH states and is obtained using Eq. (1) as well as the SCH lifetime width of 270 meV. For this case, there is, as expected, excellent agreement between the experimental observations and the theoretical predictions.

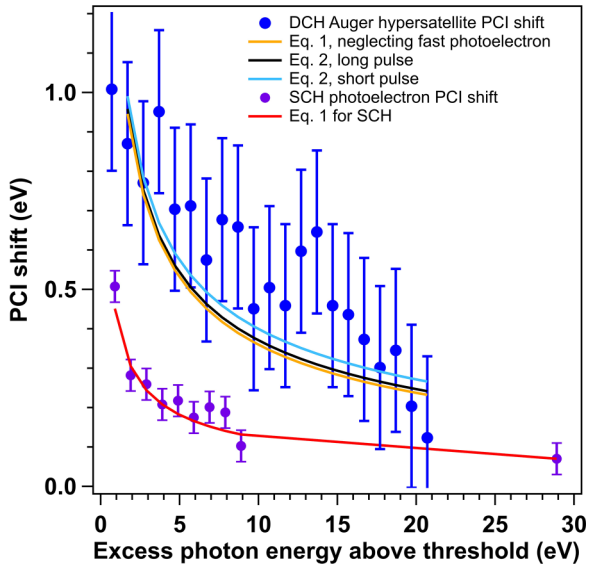


FIG. 6. Energy shifts of peak positions from the expected values for DCH hypersatellite Auger lines (measured at the SQS beamline) and SCH photoelectron lines of Ne (measured at the PLEIADES beamline) relative to their respective thresholds. Solid lines show the calculated PCI shifts using Eqs. (1) and (2) for DCH. For the SCH case, the fit is performed using Eq. (1) only. The lowest excess energies for which the solid lines are plotted indicate the energy above which the eikonal approximation is valid. The error bars represent the standard deviation of the peak positions as obtained from the fit analysis.

For the DCH states, the situation is more complicated since (1) two photoelectrons and one Auger electron are involved, and (2) these two photoelectrons are not necessarily created at the same time due to the absorption of two photons. The influence of this time delay can be taken into account in a simple way only for the extreme cases, namely, for x-ray pulse durations much longer and much shorter than the core-hole lifetime. To study the influence of the first, faster photoelectron, the orange line in Fig. 6 represents the calculated PCI shift of the slower electron by using a lifetime broadening of $\Gamma = 700$ meV and neglecting the faster one completely. The light blue curve is based on Eq. (2) with zero time delay, i.e., represents the emission of both photoelectrons with a short pulse compared to the Ne $1s$ lifetime. Finally, the black curve uses Eq. (2) and an effective lifetime for the fast photoelectron, i.e., for the case of a pulse length long compared to the neon core-hole lifetime.

In the present case, all three calculated PCI curves agree well within the error bars with the experimental data (blue dots); i.e., no influence of the faster photoelectron can be confirmed experimentally. However, we performed similar calculations assuming two photons of identical energy to populate Ar $1s^{-2}$ and Kr $1s^{-2}$ DCH states. For neon (see Fig. 6), we found a difference of about $\approx$10 meV between the curve where the fast photoelectron is neglected (orange curve) and the curve where both photoelectrons are taken into account, assuming a long pulse (black curve). For argon and krypton, these differences amount to $\approx$28 and $\approx$113 meV, respectively. For neon, the difference between the curves for long pulse (black curve) and short pulse (light blue curve) amounts to $\approx$30 meV, but becomes $\approx$85 and $\approx$340 meV for argon and krypton, respectively. These numbers show that the effect of the fast electron and, in particular, the influence of the pulse length of the x-ray radiation, increases with the atomic number and should be detectable in future experiments.

IV. CONCLUSIONS AND OUTLOOK

We present Auger hypersatellite spectra of Ne DCH states, which are populated via a sequential two-photon absorption process. These measurements are performed with monochromatized radiation provided by the European XFEL, leading to high spectral resolution. This high resolution, as well as the tunable photon energy, allows to populate selectively different singly ionized $1s^{-2}np$ DCH states and doubly ionized $1s^{-2}$ DCH states, as well as to select different population pathways, as discussed recently for water by Ismail *et al.* [9]. In pathway A, the first photon leads to a $1s$ ionization, and the second photon, depending on the photon energy, to a resonant $1s \rightarrow np$ excitation or to a second $1s$ ionization. In pathway B, the first ionization process is accompanied by a shakeup process of a $2p$ electron into a higher np Rydberg state or a shakeoff process into the continuum, followed by a resonant $1s \rightarrow 2p$ excitation in the second step.

The present data show that the most intense spectral decay feature via pathway A originates from the $1s^{-2}3p$ DCH state, whereas via pathway B it originates from the $1s^{-2}$ DCH state. This can be understood as follows. In pathway A, for all final states, the first step is identical, and in the second step, the resonant $1s \rightarrow 3p$ excitation is the most intense one. In pathway B, in the first step, shakeoff is more intense than shakeup, while in the second step, the $1s \rightarrow 2p$ excitation is practically identical for all final states.

In the case of pathway B, the intermediate $1s^{-1}2p^{-1}(n, \epsilon)p$ states can be distinguished into two groups, namely, those where $1s^{-1}$ and $2p^{-1}$ holes form a singlet or a triplet. Here, the present high-resolution measurements show that DCH states can be populated only via configurations in which the two holes form a singlet. This finding can readily be explained with the dipole selection rules for spins and is expected to be present also in molecular systems, although in the latter case, the electronic structure is more complex and the effect is probably masked by overlapping excitations.

Concerning pathways A and B, we also discussed differences for atoms and molecules. These differences are due to the fact that in an atom, the occupied orbitals $\tilde{\mathrm{V}} = 2p$ are fully occupied and the virtual orbitals $\mathrm{V} = np$, with $n \geqslant 3$ are unoccupied. In molecules, $\tilde{\mathrm{V}}$ orbitals with different term values exist. Moreover, not only the orbitals $\tilde{\mathrm{V}}$ but also the orbitals V can be $2p$ derived, so that the interaction of these both can be substantially different from that in atoms.

This work provides the first controlled experimental access to PCI in a four-body system, namely, a fast Auger electron, two photoelectrons, and a remaining ion, with tunable electron energies. In this case, the $1s^{-2}$ DCH state was prepared via pathway A, which allows us to obtain two photoelectrons with well-defined velocities, namely, a slow one and one with medium velocity. For the slow photoelectron, the kinetic energy was tuned by the photon energy between 0

and 20 eV. The observed PCI shifts agree reasonably well with calculations based on the eikonal approximation, and the PCI shift is dominated by the short DCH lifetime and the interaction of the slow photoelectron. The interaction between the Auger electron and the faster photoelectron leads only to a minor, however, not negligible correction of the PCI shift. The present calculations show an influence of the x-ray pulse length on the PCI shifts of the Auger electron, which in the present case is minor. However, calculations also show that the effect increases for heavier atoms. An additional significant increase can be expected in two-color experiments, which allow to produce two slow photoelectrons. Finally, two x-ray pulses with variable polarization direction may produce photoelectrons with selected preferential directions and may allow, in the future, to study angular-dependent effects in the four-body postcollision interaction effect.

ACKNOWLEDGMENTS

We acknowledge the European XFEL in Schenefeld, Germany, for the provision of x-ray free-electron laser beamtime at SQS under Proposal No. 2905, and we thank the staff for their support during the experiment. A portion of this research was conducted using the PLEIADES beamline at the SOLEIL synchrotron radiation facility (France), where the measurements were carried out under in-house Proposal No. 99210159. We gratefully acknowledge SOLEIL for providing synchrotron radiation infrastructure and support. We further thank E. Robert, A. Milosavljevic, and C. Nicolas for their valuable technical assistance during the PLEIADES beamtime. F.T. acknowledges funding from the Deutsche Forschungsgemeinschaft (DFG, German Research Foundation) under Project No. 509471550 (Emmy Noether Programme). Work by G.D., L.Y., and S.H.S. was supported by the U.S. Department of Energy, Office of Science, Basic Energy Sciences, Chemical Sciences, Geosciences, and Biosciences Division under Contract No. DE-AC02-06CH11357.

DATA AVAILABILITY

The neon DCH data recorded at the European XFEL that support the findings of this study are publicly available [45]. The neon SCH data that support the findings of this study are not publicly available because their dissemination is not technically feasible, and hosting the data would be prohibitive within the scope of the research project. The SCH data are available from the authors upon reasonable request.

APPENDIX: SIMPLE FORMULA FOR PCI SHIFT

The energy shift observed in the Auger electron spectrum due to PCI is fundamentally a dynamic exchange of potential energy between the final-state electron and the ion. Within the eikonal approximation, we can obtain the energy shift due to the PCI effect. This Appendix derives the simple formula used to obtain the PCI shift.

In the eikonal approximation-based model, the energy shift ΔE is calculated based on the change in the Coulomb energy for the fast Auger electron as it overtakes the slow photoelectron in the ionic field shown in Eq. (1). Under the approximation where the Auger electron has much higher kinetic energy than the photoelectron, Eq. (1) can be written as

$$\Delta E = C\frac{e^2}{4\pi\epsilon_0\hbar}\frac{\Gamma_A}{2}\frac{1}{v_{\rm ph}}. \tag{A1}$$

If we multiply the numerator and denominator of Eq. (A1) by the speed of light, $c \approx 3\times10^8$ m/s, we obtain

$$\Delta E = C\frac{e^2}{4\pi\epsilon_0\hbar c}\frac{\Gamma_A}{2}\frac{c}{v_{\rm ph}}. \tag{A2}$$

With $e^2/4\pi\epsilon_0\hbar c = \alpha \approx 1/137$ being the fine-structure constant and $v_{\rm ph} = \sqrt{2E_{\rm ph}/m_e}$ (m_e is the rest mass of the electron), we obtain

$$\Delta E = C\alpha\frac{\Gamma_A}{2}\frac{c}{v_{\rm ph}} = C\frac{\Gamma_A}{2}\sqrt{\frac{\alpha^2 m_e c^2}{2E_{\rm ph}}}. \tag{A3}$$

With $m_e c^2 \approx 0.511$ MeV and $\alpha^2 m_e c^2/2 \approx 13.6$ eV being the Rydberg constant, we obtain for the PCI shift

$$\Delta E\ ({\rm eV}) \approx C\frac{\Gamma_A[{\rm eV}]}{2}\sqrt{\frac{13.6}{E_{\rm ph}[{\rm eV}]}}, \tag{A4}$$

where all values are given in electron volts.

[1] G. Goldsztejn, T. Marchenko, R. Püttner, L. Journel, R. Guillemin, S. Carniato, P. Selles, O. Travnikova, D. Céolin, A. F. Lago, R. Feifel, P. Lablanquie, M. N. Piancastelli, F. Penent, and M. Simon, Double-core-hole states in neon: Lifetime, post-collision interaction, and spectral assignment, Phys. Rev. Lett. **117**, 133001 (2016).

[2] J. P. Cryan, J. M. Glownia, J. Andreasson, A. Belkacem, N. Berrah, C. I. Blaga, C. Bostedt, J. Bozek, C. Buth, L. F. DiMauro, *et al.*, Auger electron angular distribution of double core-hole states in the molecular reference frame, Phys. Rev. Lett. **105**, 083004 (2010).

[3] R. Guillemin, S. Sheinerman, C. Bomme, L. Journel, T. Marin, T. Marchenko, R. K. Kushawaha, N. Trcera, M. N. Piancastelli, and M. Simon, Ultrafast dynamics in postcollision interaction after multiple Auger decays in argon 1*s* photoionization, Phys. Rev. Lett. **109**, 013001 (2012).

[4] T. Marchenko, L. Inhester, G. Goldsztejn, O. Travnikova, L. Journel, R. Guillemin, I. Ismail, D. Koulentianos, D. Céolin, R. Püttner, M. N. Piancastelli, and M. Simon, Ultrafast nuclear dynamics in the doubly-core-ionized water molecule observed via Auger spectroscopy, Phys. Rev. A **98**, 063403 (2018).

[5] T. Mazza, M. Ilchen, M. D. Kiselev, E. V. Gryzlova, T. M. Baumann, R. Boll, A. De Fanis, P. Grychtol, J. Montaño, V. Music, *et al.*, Mapping resonance structures in transient core-ionized atoms, Phys. Rev. X **10**, 041056 (2020).

[6] G. Kastirke, M. S. Schöffler, M. Weller, J. Rist, R. Boll, N. Anders, T. M. Baumann, S. Eckart, B. Erk, A. De Fanis, *et al.*, Double core-hole generation in O_2 molecules using an x-ray

free-electron laser: Molecular-frame photoelectron angular distributions, Phys. Rev. Lett. **125**, 163201 (2020).

[7] I. Ismail, L. Inhester, T. Marchenko, F. Trinter, A. Verma, A. De Fanis, A. Ferté, D. E. Rivas, D. Peng, D. Koulentianos, *et al.*, Ultrafast nuclear dynamics in double-core-ionized water molecules, Phys. Rev. A **110**, 013108 (2024).

[8] N. Berrah, L. Fang, B. Murphy, T. Osipov, K. Ueda, E. Kukk, R. Feifel, P. van der Meulen, P. Salen, H. T. Schmidt, R. D. Thomas, M. Larsson, R. Richter, K. C. Prince, J. D. Bozek, C. Bostedt, S. Wada, M. N. Piancastelli, M. Tashiro, and M. Ehara, Double-core-hole spectroscopy for chemical analysis with an intense x-ray femtosecond laser, Proc. Natl. Acad. Sci. USA **108**, 16912 (2011).

[9] I. Ismail, A. Ferté, F. Penent, R. Guillemin, D. Peng, T. Marchenko, O. Travnikova, L. Inhester, R. Taïeb, A. Verma, *et al.*, Alternative pathway to double-core-hole states, Phys. Rev. Lett. **131**, 253201 (2023).

[10] S. Carniato, R. Püttner, I. Ismail, D. Peng, O. Travnikova, T. Marchenko, R. Guillemin, D. Céolin, A. Verma, N. Velasquez, M. Meyer, M. N. Piancastelli, and M. Simon, From ground to excited state: Revealing bond polarity change via $K^{-2}V$ spectroscopy and Brillouin inverse theorem (BIT), J. Phys. Chem. Lett. **16**, 9362 (2025).

[11] F. Trinter, L. Inhester, R. Püttner, S. Malerz, S. Thürmer, T. Marchenko, M. N. Piancastelli, M. Simon, B. Winter, and U. Hergenhahn, Radiationless decay spectrum of O 1*s* double core holes in liquid water, J. Chem. Phys. **160**, 194503 (2024).

[12] L. S. Cederbaum, F. Tarantelli, A. Sgamellotti, and J. Schirmer, On double vacancies in the core, J. Chem. Phys. **85**, 6513 (1986).

[13] T. D. Thomas, Single and double core-hole ionization energies in molecules, J. Phys. Chem. A **116**, 3856 (2012).

[14] R. D. Cowen, *The Theory of Atomic Structure and Spectra* (University of California Press, Berkeley, 1981).

[15] Y. Hikosaka, P. Lablanquie, F. Penent, T. Kaneyasu, E. Shigemasa, J. H. D. Eland, T. Aoto, and K. Ito, Double photoionization into double core-hole states in Xe, Phys. Rev. Lett. **98**, 183002 (2007).

[16] O. Takahashi, M. Tashiro, M. Ehara, K. Yamasaki, and K. Ueda, Theoretical spectroscopy on K^{-2}, $K^{-1}L^{-2}$, and L^{-2} double core hole states of SiX_4 (X = H, F, Cl, and CH_3) molecules, Chem. Phys. **384**, 28 (2011).

[17] J. H. D. Eland, M. Tashiro, P. Linusson, M. Ehara, K. Ueda, and R. Feifel, Double core hole creation and subsequent Auger decay in NH_3 and CH_4 molecules, Phys. Rev. Lett. **105**, 213005 (2010).

[18] P. Lablanquie, F. Penent, J. Palaudoux, L. Andric, P. Selles, S. Carniato, K. Bučar, M. Žitnik, M. Huttula, J. H. D. Eland, E. Shigemasa, K. Soejima, Y. Hikosaka, I. H. Suzuki, M. Nakano, and K. Ito, Properties of hollow molecules probed by single-photon double ionization, Phys. Rev. Lett. **106**, 063003 (2011).

[19] P. Schmüser, M. Dohlus, J. Rossbach, and C. Behrens, *Free-Electron Lasers in the Ultraviolet and X-Ray Regime* (Springer, Cham, 2014).

[20] T. Mazza, T. M. Baumann, R. Boll, A. De Fanis, S. Dold, M. Ilchen, T. Mullins, Y. Ovcharenko, D. E. Rivas, B. Senfftleben, S. Usenko, I. Ismail, J. D. Bozek, M. Simon, S. Fritzsche, and M. Meyer, Resonant Raman Auger spectroscopy on transient core-excited Ne ions, J. Phys. B: At. Mol. Opt. Phys. **57**, 225001 (2024).

[21] E. Pelimanni, A. E. A. Fouda, P. J. Ho, T. M. Baumann, S. I. Bokarev, A. De Fanis, S. Dold, G. Grell, I. Ismail, D. Koulentianos, T. Mazza, M. Meyer, M.-N. Piancastelli, R. Püttner, D. E. Rivas, B. Senfftleben, M. Simon, L. Young, and G. Doumy, Observation of molecular resonant double-core excitation driven by intense x-ray pulses, Commun. Phys. **7**, 341 (2024).

[22] M. D. Kiselev, E. V. Gryzlova, S. M. Burkov, O. Zatsarinny, and A. N. Grum-Grzhimailo, Mechanisms of 1*s* double-core-hole excitation and decay in neon, Atoms **9**, 114 (2021).

[23] M. Y. Kuchiev and S. A. Sheinerman, Post-collision interaction in atomic processes, Sov. Phys. Usp. **32**, 569 (1989).

[24] R. Guillemin, S. Sheinerman, R. Püttner, T. Marchenko, G. Goldsztejn, L. Journel, R. K. Kushawaha, D. Céolin, M. N. Piancastelli, and M. Simon, Postcollision interaction effects in *KLL* Auger spectra following argon 1*s* photoionization, Phys. Rev. A **92**, 012503 (2015).

[25] A. Niehaus, Analysis of post-collision interactions in Auger processes following near-threshold inner-shell photoionization, J. Phys. B: Atom. Mol. Phys. **10**, 1845 (1977).

[26] M. Y. Kuchiev and S. A. Sheĭnerman, Resonant processes involving the production of three charged particles, Zh. Eksp. Teor. Fiz. **90**, 1680 (1986) [Sov. Phys. JETP **63**, 986 (1986)].

[27] V. Schmidt, Experimental aspects, in *Electron Spectrometry of Atoms using Synchrotron Radiation, Cambridge Monographs on Atomic, Molecular and Chemical Physics* (Cambridge University Press, Cambridge, UK, 1997), pp. 97–184.

[28] N. Velasquez, O. Travnikova, R. Guillemin, I. Ismail, L. Journel, J. B. Martins, D. Koulentianos, D. Céolin, L. Fillaud, M. L. M. Rocco, R. Püttner, M. N. Piancastelli, M. Simon, S. Sheinerman, L. Gerchikov, and T. Marchenko, Generalization of the post-collision interaction effect from gas-phase to solid-state systems demonstrated in thiophene and its polymers, Phys. Rev. Res. **5**, 013048 (2023).

[29] S.-M. Huttula, P. Lablanquie, L. Andric, J. Palaudoux, M. Huttula, S. Sheinerman, E. Shigemasa, Y. Hikosaka, K. Ito, and F. Penent, Decay of a 2*p* inner-shell hole in an Ar^+ ion, Phys. Rev. Lett. **110**, 113002 (2013).

[30] R. Püttner, Y. Li, J. Zeng, D. Koulentianos, T. Marchenko, R. Guillemin, L. Journel, O. Travnikova, M. Zmerli, D. Céolin, Y. Azuma, S. Kosugi, M. N. Piancastelli, and M. Simon, Argon $1s^{-2}$ Auger hypersatellites, J. Phys. B: At. Mol. Opt. Phys. **54**, 024001 (2020).

[31] W. Decking, S. Abeghyan, P. Abramian, A. Abramsky, A. Aguirre, C. Albrecht, P. Alou, M. Altarelli, P. Altmann, K. Amyan, *et al.*, A MHz-repetition-rate hard x-ray free-electron laser driven by a superconducting linear accelerator, Nat. Photonics **14**, 391 (2020).

[32] D. La Civita, N. Gerasimova, H. Sinn, and M. Vannoni, SASE3: Soft x-ray beamline at European XFEL, *X-Ray Free-Electron Lasers: Beam Diagnostics, Beamline Instrumentation, and Applications II* (SPIE, Bellingham, Washington, 2014), Vol. 9210, p. 921002.

[33] T. Mazza, T. M. Baumann, R. Boll, A. De Fanis, P. Grychtol, M. Ilchen, J. Montaño, V. Music, Y. Ovcharenko, N. Rennhack, *et al.*, The beam transport system for the Small Quantum Systems instrument at the European XFEL: Optical layout and

first commissioning results, J. Synchrotron Radiat. **30**, 457 (2023).

[34] N. Gerasimova, D. La Civita, L. Samoylova, M. Vannoni, R. Villanueva, D. Hickin, R. Carley, R. Gort, B. E. Van Kuiken, P. Miedema, L. Le Guyarder, L. Mercadier, G. Mercurio, J. Schlappa, M. Teichman, A. Yaroslavtsev, H. Sinn, and A. Scherz, The soft x-ray monochromator at the SASE3 beamline of the European XFEL: From design to operation, J. Synchrotron Radiat. **29**, 1299 (2022).

[35] A. De Fanis, M. Ilchen, A. Achner, T. M. Baumann, R. Boll, J. Buck, C. Danilevsky, S. Esenov, B. Erk, P. Grychtol, *et al.*, High-resolution electron time-of-flight spectrometers for angle-resolved measurements at the SQS instrument at the European XFEL, J. Synchrotron Radiat. **29**, 755 (2022).

[36] Synchrotron SOLEIL, PLÉIADES ultra high resolution soft x-ray beamline, https://www.synchrotron-soleil.fr/en/beamlines/pleiades.

[37] F. Gel'mukhanov and H. Ågren, Raman, non-Raman, and anti-Raman dispersion in resonant x-ray scattering spectra of molecules, Phys. Rev. A **54**, 3960 (1996).

[38] E. Kukk, H. Aksela, A. Kivimäki, J. Jauhiainen, E. Nõmmiste, and S. Aksela, Electronic-state lifetime interference in the resonant Auger decay of krypton, Phys. Rev. A **56**, 1481 (1997).

[39] S. Svensson, B. Eriksson, N. Mårtensson, G. Wendin, and U. Gelius, Electron shake-up and correlation satellites and continuum shake-off distributions in x-ray photoelectron spectra of the rare gas atoms, J. Electron Spectrosc. Relat. Phenom. **47**, 327 (1988).

[40] L. Avaldi, G. Dawber, R. Camilloni, G. C. King, M. Roper, M. R. F. Siggel, G. Stefani, M. Zitnik, A. Lisini, and P. Decleva, Measurement of Ne 1*s* and 1*snl* satellite photoelectron spectra near threshold, Phys. Rev. A **51**, 5025 (1995).

[41] L. Young, E. P. Kanter, B. Krässig, Y. Li, A. M. March, S. T. Pratt, R. Santra, S. H. Southworth, N. Rohringer, L. F. DiMauro, *et al.*, Femtosecond electronic response of atoms to ultra-intense x-rays, Nature (London) **466**, 56 (2010).

[42] M. Coreno, L. Avaldi, R. Camilloni, K. C. Prince, M. de Simone, J. Karvonen, R. Colle, and S. Simonucci, Measurement and *ab initio* calculation of the Ne photoabsorption spectrum in the region of the *K* edge, Phys. Rev. A **59**, 2494 (1999).

[43] L. Gerchikov and S. Sheinerman, Post-collision-interaction distortion of low-energy photoelectron spectra associated with double Auger decay, Phys. Rev. A **84**, 022503 (2011).

[44] S. Li, D. Koulentianos, S. H. Southworth, G. Doumy, L. Young, D. A. Walko, R. Püttner, J. D. Bozek, D. Céolin, A. Verma, R. Guillemin, M. N. Piancastelli, M. Simon, L. G. Gerchikov, and S. A. Sheinerman, Manifestation of postcollision interaction in krypton *LMN* Auger spectra following *K*-shell photoionization, Phys. Rev. A **106**, 023110 (2022).

[45] M. N. Piancastelli, M. Simon, T. Baumann, *et al.*, Sequential core ionization – core excitation in the SF_6 molecule: Dynamical aspects (2022), https://doi.org/10.22003/XFEL.EU-DATA-002905-00.